Open Ceramics 27 (2026) 101009

Contents lists available at ScienceDirect

Open Ceramics

journal homepage: www.sciencedirect.com/journal/open-ceramics

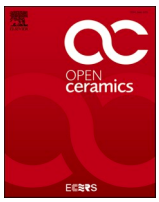

Architectural engineering of reduced graphene oxide in $BiVO_4$ photoanodes for enhanced photoelectrochemical performance

Marko Jelić [a,*], Zoran Jovanović [a], Suraj Gupta [b], Danica Bajuk-Bogdanović [c], Srečo Škapin [b], Zhao Liang [d], Matjaž Spreitzer [b], Sonja Jovanović [a,*]

[a] Vinča Institute of Nuclear Sciences – National Institute of the Republic of Serbia, University of Belgrade, Mike Petrovića Alasa 12-14, Belgrade, Serbia
[b] Advanced Materials Department, Jožef Stefan Institute, Jamova 39, Ljubljana, Slovenia
[c] University of Belgrade-Faculty of Physical Chemistry, Studentski Trg 12-16, 11158 Belgrade, Serbia
[d] Institute of Micro/Nano Materials and Devices, Ningbo University of Technology, Ningbo, 315211, China

ARTICLE INFO

Keywords:
Bismuth vanadate
Reduced graphene oxide
Photoelectrochemistry
Water-splitting
Heterointerfaces

ABSTRACT

Bismuth vanadate ($BiVO_4$) is a promising photoanode material for solar water splitting due to its visible-light absorption and earth-abundant composition. Herein, we investigate how the spatial positioning of reduced graphene oxide (rGO) influences the photoelectrochemical performance of hydrothermally synthesized $BiVO_4$ photoanodes. Two heterostructures were examined, with rGO incorporated either beneath the $BiVO_4$ layer (BVO/rGO/FTO) or on the surface (rGO/BVO/FTO). Both architectures exhibit enhanced photocurrent densities compared to pristine $BiVO_4$. Surface-deposited rGO primarily improves interfacial charge extraction, resulting in the highest photocurrent and interfacial efficiencies exceeding 25–30%. In contrast, buried rGO enhances bulk charge separation and electron transport, leading to a nearly twofold increase in charge-transport efficiency and an fourfold enhancement in photovoltage. IPCE values increased by more than one order of magnitude relative to pristine $BiVO_4$, demonstrating the importance of heterointerface engineering for optimizing charge-transfer pathways in ceramic photoanodes.

1. Introduction

Photoelectrochemical (PEC) water splitting is widely regarded as a promising strategy for sustainable solar-to-chemical energy conversion [1]. Among visible-light-responsive oxide semiconductors, monoclinic bismuth vanadate ($BiVO_4$, BVO) has emerged as one of the most attractive photoanode materials due to its suitable bandgap (~2.4 eV), favorable valence band position for oxygen evolution, chemical stability, and earth-abundant composition [2]. Nevertheless, the practical PEC performance of BVO remains severely constrained by intrinsic limitations, including low bulk conductivity, short carrier diffusion lengths, and pronounced charge recombination at both bulk and surface sites [3].

To overcome these limitations, extensive efforts have been devoted to improving charge separation and transport in BVO through strategies such as doping, heterojunction formation, defect engineering, morphology control, and surface modification [4–7]. Among these approaches, coupling BVO with graphene oxide-based conductive materials has attracted considerable attention [8,9]. Reduced graphene oxide (rGO), in particular, has been widely explored due to its high electrical conductivity, large specific surface area, and ability to act as an efficient electron acceptor and transport medium [10]. rGO has been extensively investigated as a co-catalyst and charge-transport scaffold in photocatalytic systems due to its excellent electron conductivity, high specific surface area, and ability to facilitate charge separation when coupled with semiconductors. In particular, coupling semiconductor photocatalysts with rGO has been shown to enhance charge carrier separation and suppress recombination, often leading to significantly improved photocatalytic activity under visible light irradiation [11–14]. Early studies demonstrated that, compared to the pristine BVO, rGO/BVO hybrid systems can significantly enhance visible-light photoactivity and PEC water splitting performance by prolonging electron lifetimes and suppressing charge recombination [15].

Subsequent reports further confirmed that rGO/BVO composites exhibit improved photocurrent densities, enhanced charge transfer properties, and increased stability across a range of photocatalytic and photoelectrochemical applications [16–18]. Beyond the simple addition of rGO, increasing evidence suggests that the efficiency of rGO/BVO

* Correponding authors.
E-mail addresses: marko.jelic@vin.bg.ac.rs (M. Jelić), sonja.jovanovic@vin.bg.ac.rs (S. Jovanović).

https://doi.org/10.1016/j.oceram.2026.101009
Received 19 May 2026; Received in revised form 10 June 2026; Accepted 25 June 2026
Available online 26 June 2026

systems is strongly governed by the nature of the interfacial interaction between the two components. Studies employing electrostatic self-assembly or engineered interfacial coupling have shown that contact between BVO and rGO can substantially enhance charge separation efficiency and interfacial electron transfer, leading to improved visible-light photocatalytic activity [19,20]. Moreover, it has been shown that the charge-shuttling behavior of rGO is sensitive to the local electronic structure and surface characteristics of BVO, including facet-dependent interactions that influence interfacial energetics and electron transport pathways [21].

Recent studies have demonstrated that interfacial engineering and charge-transfer mediation layers can substantially influence charge separation and water oxidation kinetics in $BiVO_4$-based photoanodes, highlighting the importance of understanding how the spatial arrangement of additional functional layers affects photoelectrochemical performance [22]. In parallel, numerous $BiVO_4$-based heterostructures and interfacial engineering strategies have been investigated to separately address limitations associated with bulk charge separation or sluggish surface water oxidation kinetics. Shao *et al.* demonstrated that Tb doping of $BiVO_4$ can promote bulk charge separation by creating an efficient "electron highway", while a CoFeMoCuOOH overlayer simultaneously accelerates surface hole extraction and oxygen evolution kinetics through multifunctional interfacial charge management [23]. In a similar study with $NiFeO_x/Tb(OH)_x/BiVO_4$ photoanode architecture, Tb $(OH)_x$ nanoparticles acted as efficient hole-extraction mediators, rapidly transferring photogenerated holes from $BiVO_4$ to the NiFeOx cocatalyst layer, thereby improving both bulk charge separation efficiency and water oxidation kinetics [24]. Also, orbital-engineered $CoFeOP/BiVO_4$ heterojunctions have been shown to enhance interfacial charge transfer and surface water oxidation kinetics by optimizing band alignment, reaction intermediate adsorption, and carrier dynamics at the semiconductor/cocatalyst interface [25]. Similarly, the incorporation of polycarbazole hole-transport layers and NiFeOOH cocatalysts on $BiVO_4$ photoanodes has been shown to synergistically enhance interfacial hole extraction and surface water oxidation kinetics, leading to substantially improved photoelectrochemical performance [26].

However, similar mechanistic considerations regarding the spatial positioning of rGO within $BiVO_4$ heterostructures remain largely unexplored. The majority of literature reports about rGO/BVO systems still treat rGO as a generic conductive additive, with limited attention paid to its positioning within the heterostructure. In particular, systematic investigations correlating the location of rGO relative to the semiconductor absorber with interfacial charge-transfer behavior, surface chemical evolution during PEC operation, and long-term structural stability remain scarce. Overlooking the architecture of the heterostructure limits a fundamental understanding of how its spatial positioning of layers controls charge extraction and recombination processes under realistic operating conditions. Depending on its location, rGO can interact with $BiVO_4$ in fundamentally different ways: when placed at the back contact, rGO may primarily enhance bulk electron extraction and reduce recombination within the semiconductor, whereas surface-deposited rGO can influence interfacial charge transfer, surface states, and reaction kinetics. Disentangling these effects is crucial for rational electrode design but is often overlooked, as many reports focus on rGO incorporation without explicitly addressing architectural control.

In this work, we address this gap by systematically investigating BVO photoanodes modified with rGO being deposited beneath (BVO/rGO/FTO) and on top of the BVO layer (rGO/BVO/FTO). By combining photoelectrochemical measurements, spectral efficiency analysis, and post-operando structural and surface characterization, we elucidate how location of rGO affects charge transfer dynamics, structural, optical and surface chemistry evolution in neutral phosphate buffer. We show that placement of rGO at the back contact (BVO/rGO/FTO) predominantly improves bulk charge separation and electron transport, leading to an approximately twofold increase in charge-transport efficiency compared to pristine $BiVO_4$. In contrast, surface-deposited rGO (rGO/BVO/FTO) primarily enhances interfacial charge extraction, doubling the interfacial efficiency and effectively suppressing surface recombination. These results provide new insights into spatially engineered rGO–oxide interfaces and offer guidelines for other 2D materials in designing durable ceramic photoanodes for solar water splitting.

2. Experimental methods

2.1. Chemicals

Bismuth (III) nitrate pentahydrate ($(Bi(NO_3)_3{\cdot}5H_2O$, ACS reagent, Acros Organics), ammonium mono-vanadate (NH_4VO_3, Carl Roth, 99.8%), Poly(vinyl alcohol) (88% hydrolyzed, average M.W. 85000–120000), 65% nitric acid (HNO_3, Avantor Macron), graphene oxide (Advanced Graphene Products, 4 mg/ml), ethanol (Reahem), Milli-Q deionized water.

2.2. Preparation of the $BiVO_4$ seed layer on FTO

The synthesis procedure of BVO was carried out using a slightly modified version of the previously reported protocol [6]. For the seed layer formation, the precursor solution was prepared by dissolving 0.6486 g of $Bi(NO_3)_3{\cdot}5H_2O$ in 2 mL of concentrated HNO_3, followed by the addition of 4 mL of Milli-Q water and 0.1570 g of NH_4VO_3. After thorough mixing for 30 min, 0.3354 g of poly(vinyl alcohol) (PVA) was added and dissolved using ultrasonication. Prior to deposition, Fluorine-doped tin oxide (FTO) substrates were sequentially cleaned in an ultrasonic bath using toluene (10 min), acetone (10 min), ethanol (15 min), and Milli-Q water (30 min). The $BiVO_4$ seed layer was deposited via a three-step spin-coating process. In each step, 1 mL of the precursor solution was applied in 20 μL increments with 20 s intervals between steps at 8000 rpm. The first two coatings were calcined at 300 °C in air for 15 min. After cooling to room temperature, a third layer was applied under the same conditions but calcined at 450 °C for 2 h.

2.3. Preparation of the $BiVO_4$ photoanode

For hydrothermal growth, a solution was prepared by dissolving 0.1077 g of $Bi(NO_3)_3{\cdot}5H_2O$ and 0.0264 g of NH_4VO_3 in 1.5 mL of concentrated HNO_3 under magnetic stirring, followed by dilution with 55 mL of Milli-Q water. The seed-coated FTO substrates were placed at a 45° angle in a specially designed holder, with the seed layer facing downward, inside a Teflon-lined autoclave. The hydrothermal growth process was conducted at 180 °C for 24 h, after which the autoclave was naturally cooled to room temperature. The obtained films were rinsed with Milli-Q water and calcined at 450 °C for 2 h in air. This sample was denoted as BVO/FTO.

2.4. Preparation of the $BiVO_4$ photoanodes with rGO

Reduced graphene oxide (1 mg/ml) was prepared from commercial aqueous suspension of graphene oxide (GO). In both electrode architectures, GO was deposited by spin coating at 8000 rpm, using a total volume of 1 mL, applied in 20 μL portions with a 20 s pause between consecutive drops to ensure uniform film formation. Following spin coating, the deposited GO films were thermally reduced at 250 °C in an argon atmosphere for 2 h, yielding reduced graphene oxide (rGO). Temperature has been chosen as optimal for epoxy and alkoxy group removal [27].

For the sample denoted as BVO/rGO/FTO, GO was deposited directly onto the cleaned FTO substrates prior to the $BiVO_4$ seed layer deposition. After spin coating, the GO-coated FTO substrates were thermally reduced at 250 °C in an argon atmosphere for 2 h to obtain an rGO interlayer. The rGO-modified FTO substrates were subsequently used for $BiVO_4$ seed layer deposition and hydrothermal growth, following the procedures described in Sections 2.2 and 2.3.

For the rGO/BVO/FTO, GO was deposited onto fully prepared $BiVO_4$ photoanodes after hydrothermal growth and post-calcination. The $BiVO_4$ films were allowed to cool to room temperature prior to GO deposition. After spin coating of GO, the films were thermally reduced at 250 °C in an argon atmosphere for 2 h, resulting in a conformal rGO overlayer on the $BiVO_4$ surface.

3. Characterization techniques

3.1. Photoelectrochemical measurements

Photoelectrochemical (PEC) measurements were performed using a standard three-electrode configuration. The photoanodes served as the working electrodes, a platinum wire was used as the counter electrode, and an Ag/AgCl (3 M NaCl) electrode was used as the reference electrode. All PEC experiments were conducted under back-side illumination through the fluorine-doped tin oxide (FTO). Solar simulator (Newport, 66984-300XF-R1) with AM 1.5 G filter was used and incident illumination was calibrated using Si reference cell at 100 mW/cm^2. Photoelectrochemical measurements were performed in phosphate buffer (pH = 8) under simulated solar illumination. The potential scale was converted to the reference hydrogen electrode (RHE) scale using Nernst equation [28]:

$$E_{RHE} = E_{Ag/AgCl} + E^{\circ}_{Ag/AgCl} + 0.0591 \times pH \quad (1)$$

where $E^{\circ}_{Ag/AgCl} = 0.1976$ V at 25 °C (2)

For all measurements, Gamry's 1010E potentiostat was used as a workstation. Linear sweep voltammetry (LSV) was carried out in the potential window from 0 to 1.23 V vs RHE with a scan rate of 2 mV s^{-1}. Chronoamperometry measurements were performed at 1.23 V vs RHE for both short-term (chopped illumination) and long-term stability tests. Electrochemical impedance spectroscopy (EIS) measurements were conducted at a DC bias of 1.23 V vs RHE with an AC perturbation of 10 mV (rms) over a frequency range of 0.1 Hz to 10^5 Hz. Mott–Schottky measurements were performed in the potential range of 0–1 V vs RHE with a voltage step of 0.05 V at a frequency of 1000 Hz. More details related to PEC measurements and calculations can be found in Supplementary information.

3.2. Other characterization techniques

Raman spectra were obtained using DXR Raman microscope (Thermo Scientific) operating at 532 nm excitation wavelength (at 2 mW laser power) in the 50–3500 cm^{-1} range (exposure time: 10 s; spot size 2.1 μm; 3 spectra per sample). The crystal structure of materials was determined by X-ray diffraction (XRD, Bruker AXS D4 Endeavor diffractometer) with Cu K-α radiation in the range of 10 - 65° and step size 0.04°. SEM measurements were performed using Jeol JSM-7600F microscope in the secondary electron mode at an accelerating voltage of 15 kV. X-ray photoelectron spectroscopy (XPS) measurements were performed on a spot size of 200 μm using PHI Versa Probe III with Al Kα radiation (1486.6 eV). All the high-resolution data was referenced with respect to C 1 s peak at 284.8 eV. The optical properties were characterized using a Shimadzu UV-2600 UV–Vis spectrophotometer equipped with an integrating sphere.

4. Results and discussion

4.1. Structural and morphological analysis

Raman spectroscopy was employed to probe the structural properties of pristine and rGO-modified $BiVO_4$ photoanodes (Fig. 1a). The Raman spectrum is dominated by a strong band at 825 cm^{-1}, corresponding to the symmetric V–O stretching mode (A_g) of the VO_4 tetrahedra (υ_s), which is characteristic of monoclinic $BiVO_4$ [29]. A weaker feature around 715 cm^{-1} is attributed to the antisymmetric V–O stretching mode, υ_{as}, (B_g). In the intermediate region, bands at 331 and 371 cm^{-1} arise from antisymmetric (B_g) and symmetric (A_g) O–V–O bending vibrations, δ_s and δ_{as}, respectively [29]. Additional low-wavenumber bands observed at ~130 and ~215 cm^{-1} are associated with external lattice modes, corresponding to rotational and translational vibrations of the $BiVO_4$ structure (Fig. 1b) [30]. For the BVO/rGO/FTO sample, the Raman spectrum remains nearly identical to that of pristine BVO/FTO, indicating that the incorporation of rGO beneath the BVO layer does not affect the crystal structure of BVO and that the rGO signal is not detectable due to its buried position. In contrast, the rGO/BVO/FTO sample shows weak but discernible D (~1350 cm^{-1}) and G (~1580 cm^{-1}) bands (dashed rectangle in Fig. 1a), confirming the presence of rGO at the surface [31]. The reference rGO/FTO spectrum exhibits pronounced D and G bands along with a weaker 2D band (~2700 cm^{-1}). The extracted intensity ratio I_D:I_G ~ 1.2, determined from the integrated areas of the deconvoluted Raman peaks, indicates moderate structural disorder and defect density characteristic of rGO, together with reduced sp^2 graphitic domain size [32]. In addition, weaker bands at 444 cm^{-1} (E_g), 574 cm^{-1} (A_{1g}), and 1104 cm^{-1} ($E_u \times E_u$) are attributed to the

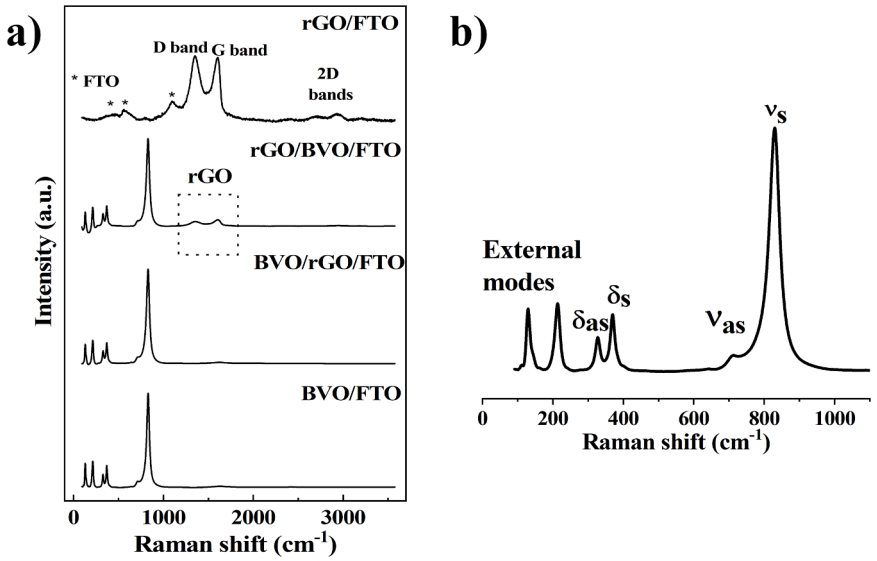

Fig. 1. a) Raman spectra of BVO/FTO and rGO modified BVO/FTO; b) magnified Raman spectrum of BVO/FTO.

underlying FTO substrate [33].

Fig. 2 represents the XRD patterns for both pristine and rGO-modified BVO films, showing diffraction maxima typical of monoclinic scheelite $BiVO_4$ along with contributions from the underlying FTO substrate (JCPDS No. 41–1445) [34]. The incorporation of rGO does not alter the bulk crystal structure of BVO, as no additional diffraction maxima are observed. The absence of distinct reflections associated with GO stacking or graphitic (002) planes indicate that rGO is present in a highly exfoliated form, without significant restacking of the nanosheets.

Pristine BVO/FTO exhibits a compact polycrystalline morphology composed of well-faceted grains with an average lateral size of approximately 600 nm, forming a relatively dense and continuous film (Fig. 3a) similarly observed for other films prepared via combination of spin coating and hydrothermal synthesis [35–37]. For the BVO/rGO/FTO architecture (Fig. 3b), a clear reduction in grain size (~200 nm average lateral size) is observed compared to pristine BVO/FTO, with a higher density of smaller and a more heterogeneous grain-size distribution. This indicates that the presence of rGO beneath the BVO layer influences the nucleation and growth process during film formation. In the case of rGO/BVO/FTO, the surface morphology remains generally similar to that of pristine BVO/FTO, with comparable grain size and faceting; while no distinct rGO features are observed, subtle contrast variations are visible, consistent with a thin and discontinuous rGO layer conformally coating the BVO surface (Fig. 3c) [21].

4.2. Surface chemical analysis by XPS

XPS measurements were performed to investigate the surface chemical composition and electronic structure of BVO and rGO modified photoanodes. The C 1 s spectra of pristine BVO/FTO are dominated by a main maximum at 284.8 eV, attributed to adventitious carbon (C–C/C═C), accompanied by higher binding energy components at ~285.9–288.6 eV corresponding to C–O and C═O species (Fig. 4 and Table S1). These contributions are commonly observed for oxide surfaces exposed to air and originate from surface contamination and weakly bound carbonate species [38,39]. For BVO/rGO/FTO, the C 1 s spectra is dominated by surface carbonaceous species associated with BVO rather than intrinsic rGO contributions, since the rGO layer is positioned beneath the BVO film and can only contribute to the XPS signal in localized regions between grains where open pathways provide access to the underlying FTO substrate supporting the rGO layer (Fig. 4b and Table S1). rGO/BVO/FTO exhibits different C 1 s spectra (Fig. 4c and Table S1) as additional high-binding-energy features at ~289–291 eV are observed, assigned to oxidized carbon species (O–C═O) and π–π* shake-up satellites, characteristic of graphitic carbon networks [40–42].

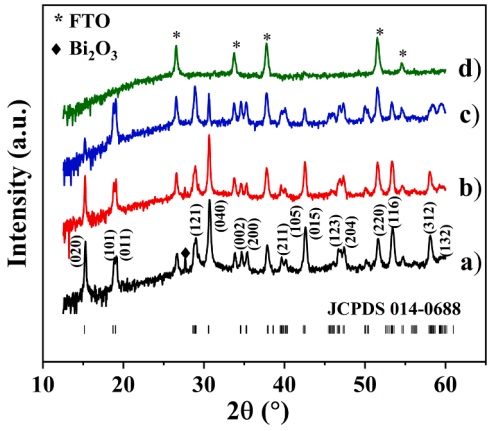

Fig. 2. XRD patterns of a) BVO/FTO, b) BVO/rGO/FTO, c) rGO/BVO/FTO and d) rGO/FTO. Only selected crystallographic planes are shown for clarity due to their large number; the complete set of reflections can be found in JCPDS card No. 014–0688.

For comparison, bare rGO exhibits a C 1 s spectrum dominated by the graphitic C–C/C═C peak at 284.8 eV with pronounced contributions from C–O, C═O, and O–C═O functional groups at higher binding energies (Fig. 4d and Table S1).

Analysis of the O 1 s spectra provides further insight into surface processes. For pristine BVO/FTO and BVO/rGO/FTO, the O 1 s envelope consists of a dominant lattice oxygen peak at ~529.7 eV (from VO_4 tetrahedron), accompanied by higher-energy components at ~531–532 eV associated with surface hydroxyl groups and adsorbed oxygen species (Fig. 4a, b and Table S1) [43]. In contrast, rGO/BVO/FTO shows a broader and more complex O 1 s spectrum, with multiple high-binding-energy components extending beyond 533 eV. These features are attributed to oxygen-containing functional groups on rGO (C–O, C═O, O–C═O) and adsorbed electrolyte species. O 1 s spectrum of rGO/FTO is composed of FTO oxygen components as well as of oxygen-containing carbon functionalities (Fig. 4d and Table S1).

The Bi 4f and V 2p spectra didn't show significant difference among the samples. The Bi 4f spectra consists of the peaks at ~159 and 164 eV which are characteristic of the spin–orbit split of Bi $4f_{7/2}$ and Bi $4f_{5/2}$, and confirms the presence of Bi^{3+} [44]. The vanadium peak that corresponds to V $2p_{3/2}$ was noticed at ~516 eV and indicates the presence of V^{5+} [44].

4.3. Photoelectrochemical performance

Photoelectrochemical measurements were performed in phosphate buffer (pH = 8) under simulated solar illumination using 3-electrode configuration. Based on LSV results, the pristine BVO photoanode exhibits relatively low photocurrent densities and a delayed photocurrent onset, indicative of inefficient charge separation and pronounced recombination under water oxidation conditions [2]. Upon incorporation of rGO, a marked improvement in photoelectrochemical activity is observed for both, rGO/BVO/FTO and BVO/rGO/FTO, confirming the beneficial role of rGO integration in enhancing charge transport and extraction (Fig. 5a). Among all investigated samples, the rGO/BVO/FTO photoanode exhibited the highest photocurrent density, reaching approximately 0.3 mA cm^{-2} at 1.23 V vs. RHE. This result highlights the beneficial role of surface-deposited rGO in facilitating interfacial charge extraction and suppressing surface recombination under higher anodic bias. Although the absolute photocurrent values are modest, they are consistent with previously reported non-doped $BiVO_4$/rGO systems measured under neutral or near-neutral electrolyte conditions in the absence of hole scavengers and catalytically active cocatalysts [15,21,40]. Also, rGO/BVO/FTO shows a distinct current–potential behavior in the low-potential region (0–0.4 V vs RHE), which is attributed to a pronounced capacitive contribution arising from electric double-layer charging and discharging associated with surface-exposed rGO [45]. On the other hand, the BVO/rGO/FTO photoanode exhibits a more favorable photocurrent onset potential, consistent with improved bulk charge separation and electron extraction facilitated by rGO at the back contact [46,47]. Control measurements of rGO deposited on FTO reveal negligible photoelectrochemical response, however, a similar current–potential behavior is observed in the low-potential region (< 0.4 V vs RHE), indicating that the capacitive features originate from the rGO layer (Fig. S1).

Several studies have demonstrated that incorporation of rGO into BVO significantly improves photoelectrochemical performance by enhancing charge separation and electron transport. Ng *et al.* reported nearly a one order of magnitude increase in photocurrent for BVO/rGO photoanodes compared to pristine BVO under visible-light illumination, attributing the improvement to efficient electron injection from BVO into rGO and improved electrical contact with the FTO substrate [15]. Tan *et al.* further showed that the photoactivity enhancement in BVO/rGO composites strongly depends on the exposed crystal facets of BVO, where increased exposure of the {010} facets promoted more efficient electron transfer to rGO due to favorable interfacial electronic

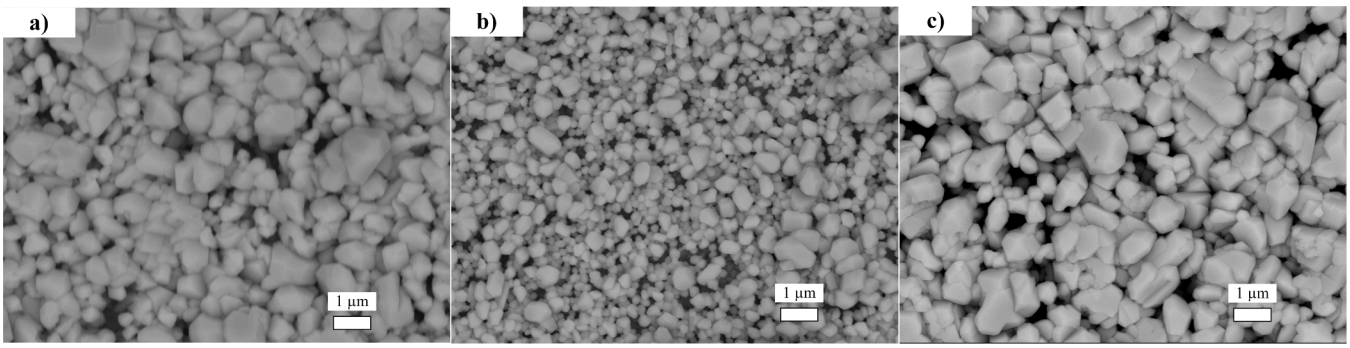

Fig. 3. SEM micrographs of a) BVO/FTO, b) BVO/rGO/FTO, and c) rGO/BVO/FTO.

structure and reduced Schottky barrier height [21]. Their work demonstrated that rGO acts as an effective electron shuttle, suppressing recombination and improving photocurrent generation through facet-dependent charge extraction. More recently, Cheng *et al.* combined alkaline-etched BVO with commercial rGO (Ultraphene™), achieving photocurrent densities as high as 5.89 mA cm^{-2} at 1.23 V vs RHE, compared to only 0.70 mA cm^{-2} for pristine BVO [18]. The enhanced performance was attributed to the synergistic effect of morphology modification, increased active-site density, improved conductivity, and accelerated interfacial charge transfer introduced by the rGO incorporation.

Electrochemical impedance spectroscopy (EIS) measurements performed under illumination provide further insight into the charge-transport and interfacial processes governing the LSV behavior (Fig. 5b). Using the equivalent circuit (Fig. S2), it has been shown that pristine BVO photoanode exhibits relatively high bulk and interfacial resistances, consistent with inefficient charge transport and pronounced recombination losses (Table 1). Similar impedance characteristics, reflecting transport limitations and significant recombination in pristine $BiVO_4$, have been widely reported in the literature [48]. Upon incorporation of rGO, both architectures show a clear reduction in charge-transfer resistance, confirming the beneficial role of rGO in facilitating charge extraction. Notably, the rGO/BVO/FTO photoanode exhibits the lowest interfacial charge-transfer resistance, indicating highly efficient surface charge extraction and interfacial kinetics, in agreement with its superior high-bias photocurrent density observed in LSV measurements and other literature reports [49]. The BVO/rGO/FTO also displays reduced resistances compared to pristine BVO, but to a lesser extent, reflecting its primary role in improving bulk electron transport rather than surface charge transfer.

The dynamic photoresponse, evaluated by chopped-light chronoamperometry (Fig. 5c), shows stable and reproducible photocurrent transients for pristine BVO/FTO and BVO/rGO/FTO, indicating efficient charge separation with minimal accumulation of surface-trapped charges. In contrast, the rGO/BVO/FTO photoanode exhibits a more pronounced decay in photocurrent during repeated on–off illumination cycles, suggesting increased charge accumulation and enhanced surface-related recombination processes associated with surface-exposed rGO. This behavior becomes even more evident during prolonged operation, where the rGO/BVO/FTO electrode shows an approximately 40% decrease in photocurrent after 2 h at 1.23 V vs. RHE (Figure S3), highlighting the limited long-term stability of these pristine $BiVO_4$/rGO-based photoanodes under the employed operating conditions. Therefore, while surface-exposed rGO effectively enhances initial charge extraction and photocurrent density, it also appears to introduce surface-sensitive degradation pathways during extended operation, emphasizing the trade-off between photoelectrochemical activity and operational stability.

Consistent with the LSV results, where rGO/BVO/FTO exhibited a pronounced capacitive contribution, transient photocurrent analysis (Eq. S1) confirms enhanced charge storage in rGO-modified photoanodes (Figure S4) [50]. The highest stored charge is observed for rGO/BVO/FTO, in agreement with its strong capacitive response, whereas BVO/rGO/FTO shows lower charge accumulation, indicating more efficient charge extraction and reduced carrier trapping. Notably, a relatively large cycle-to-cycle variation is observed for all samples, reflecting the dynamic nature of the transient response and the sensitivity of the system to time-dependent processes under illumination [51].

To further investigate the electronic properties and interfacial charge behavior of the prepared photoanodes, frequency-dependent Mott–-Schottky measurements were performed in the 500–5000 Hz range (Fig. 5d,e,f). The BVO/FTO and BVO/rGO/FTO photoanodes exhibited two distinguishable linear regions with positive slopes: the first in the lower potential region (0–0.6 V vs. RHE) and the second at higher potentials (0.6–1.6 V vs. RHE). Both regions exhibited only minor frequency-dependent variations, indicating relatively stable capacitance behavior and reasonable agreement with the assumptions of classical Mott–Schottky theory. The low-potential region is likely associated with surface states and interfacial charging processes, whereas the higher-potential region predominantly reflects the depletion capacitance of the bulk $BiVO_4$ space-charge layer [52]. A markedly different behavior was observed for the rGO/BVO/FTO photoanode, where negative slopes appeared at higher frequencies, indicating substantial interfacial charging contributions associated with the surface-exposed rGO layer. This behavior correlates well with the low-potential capacitive current response observed in the LSV measurements and further confirms the role of rGO in modifying interfacial charge accumulation and electric double-layer capacitance. Donor density and flat-band potential values were calculated from the second linear region of the Mott–Schottky plots recorded at 1000 Hz (Fig. 5d, e, f), where the response exhibited comparatively stable behavior and most closely satisfied the assumptions of classical Mott–Schottky analysis [53]. The calculated donor density values were similar to all of the 3 samples, indicating relatively similar carrier concentrations among the investigated photoanodes. In contrast, the extracted flat-band potentials exhibited noticeable differences depending on the rGO configuration. The BVO/FTO photoanode exhibited a flat-band potential of approximately 0.65 V vs. RHE, while BVO/rGO/FTO and rGO/BVO/FTO showed lower values of approximately 0.31 V and 0.30 V vs. RHE, respectively (Table 1).

Linear sweep voltammetry performed in sodium sulfite electrolyte, acting as a fast hole scavenger, yields substantially higher photocurrent densities for all photoanodes compared to measurements in phosphate buffer, confirming that water oxidation kinetics impose a significant surface reaction limitation under operating conditions (Fig. 6a) [54]. Although pristine BVO/FTO still exhibits the lowest photocurrent densities, a clear architecture-dependent trend is observed. In sulfite electrolyte, BVO/rGO/FTO delivers higher photocurrents than rGO/BVO/FTO, indicating more efficient charge collection when rGO is positioned beneath the $BiVO_4$ layer. This behavior highlights the role of

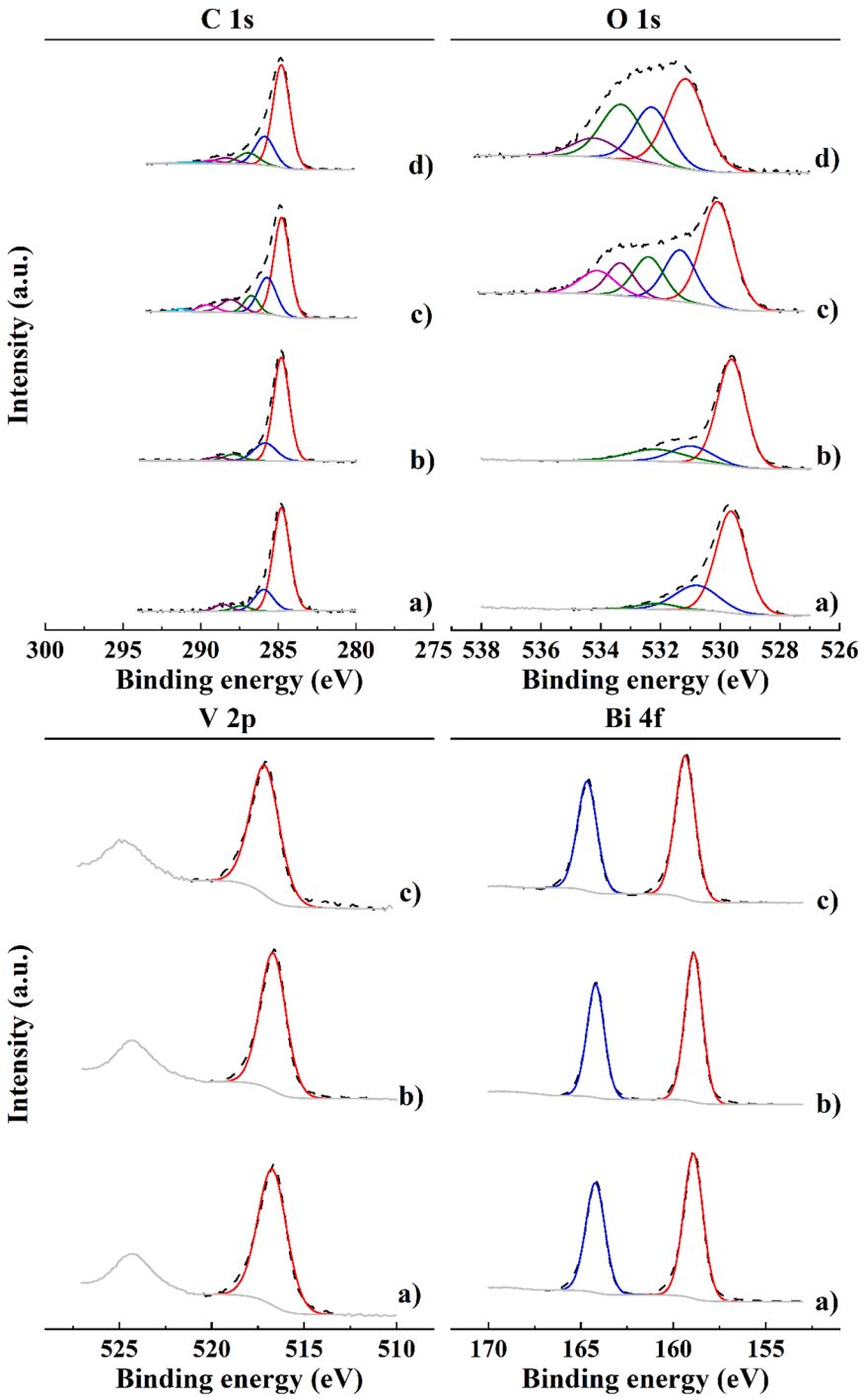

Fig. 4. C 1 s, O 1 s, V 2p and Bi 4f core-level spectra of a) BVO/FTO, b) BVO/rGO/FTO, c) rGO/BVO/FTO and d) rGO/FTO.

back-contact rGO in facilitating electron extraction and improving bulk charge separation, thereby suppressing bulk recombination, which becomes the dominant limiting factor once surface reaction kinetics are accelerated by the hole scavenger.

The difference between photocurrents measured in phosphate buffer and sodium sulfite was used to estimate the surface charge-transfer efficiency (η_i) (Fig. 6b, Eq S3-S6) [55]. Under water oxidation conditions, rGO/BVO/FTO exhibits the highest η_i over the entire potential range, consistent with highly efficient interfacial charge extraction enabled by surface-deposited rGO. In contrast, pristine BVO/FTO and BVO/rGO/FTO show lower η_i values, indicating a stronger influence of surface reaction losses. Notably, the relatively smaller photocurrent enhancement of rGO/BVO/FTO in sulfite electrolyte suggests that surface-exposed rGO does not purely act as an inert conductive pathway but may undergo partial chemical interaction or modification in the presence of sulfite species.

Incident photon-to-current efficiency (IPCE) measurements in the 350–550 nm range further corroborate the architecture-dependent charge-management mechanisms (Fig. 6c and Eq S9). Pristine BVO/FTO displays negligible IPCE values across the investigated spectrum, reflecting severe losses due to inefficient charge transport and interfacial recombination. Both rGO-modified photoanodes exhibit a pronounced enhancement in IPCE, with rGO/BVO/FTO showing the highest values (up to ~16%), indicating that efficient interfacial charge extraction

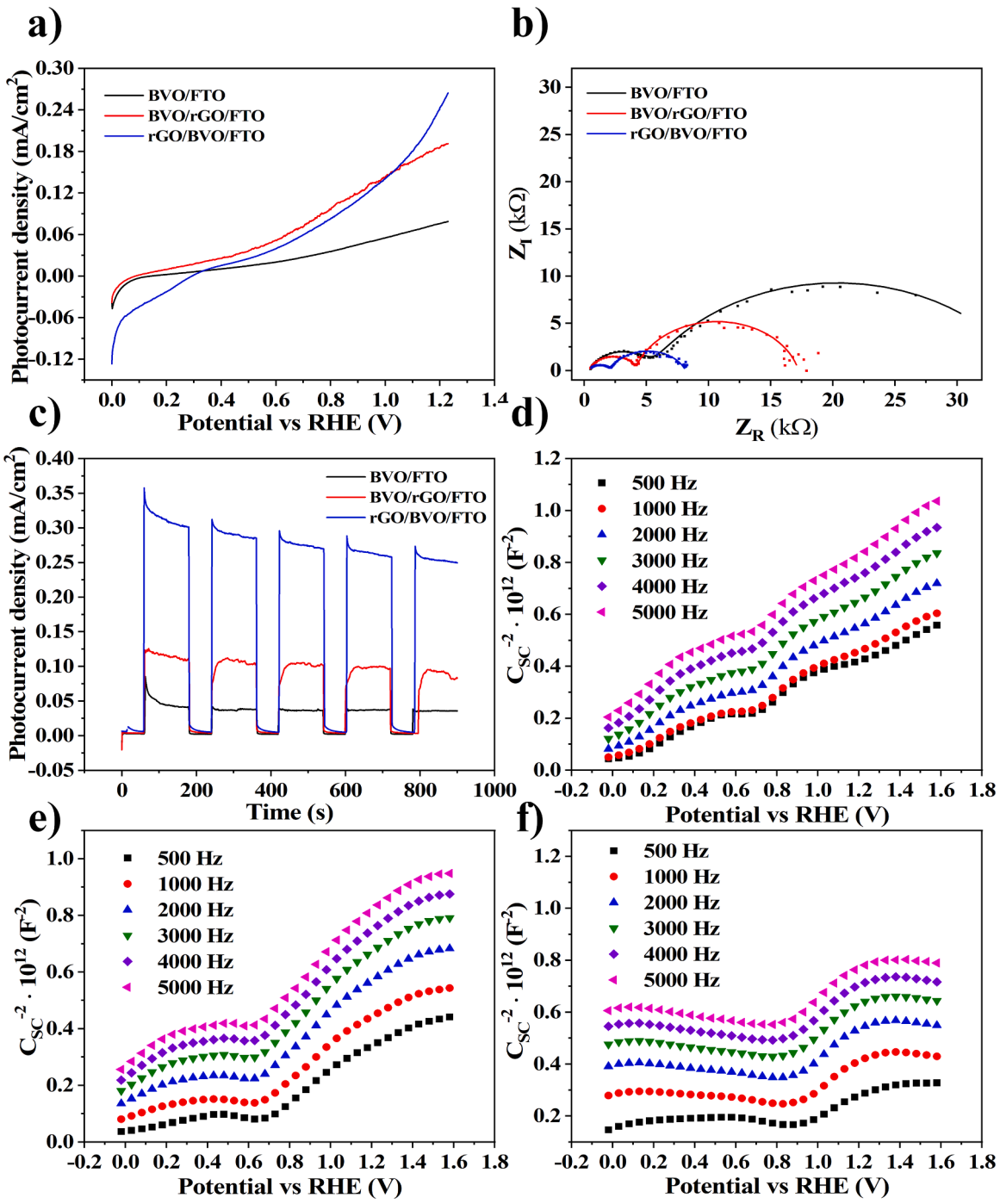

Fig. 5. PEC characterization of BVO/FTO, BVO/rGO/FTO, and rGO/BVO/FTO in 0.1 M phosphate buffer (pH = 8) using a) LSV, b) EIS, c) chopped-light chronoamperometry and d) Mott-Schottky analysis. The frequency-dependent Mott–Schottky measurements performed in the 500–5000 Hz range for d) BVO/FTO, e) BVO/rGO/FTO and f) rGO/BVO/FTO.

Table 1
Results of EIS and MS fitting in the 0.1 M phosphate buffer.

Sample	R_e (Ω)	R_{bulk} (kΩ)	$R_{surface}$ (kΩ)	N_D (cm^{-3} $\cdot 10^{19}$)	V_{FB} vs RHE (V)
BVO/FTO	456	30.2	4.8	7.1	0.65
BVO/rGO/FTO	443	13.1	3.7	5.7	0.31
rGO/BVO/FTO	397	6.1	1.7	6.1	0.30

effectively mitigates surface recombination once sufficient bulk transport is achieved. The sharp decrease in IPCE above ~500 nm is consistent with the absorption edge of $BiVO_4$ (Figure S5). A similar trend in the efficiency improvements was observed in other literature reports related to the rGO-modified $BiVO_4$ [9,56,57].

Applied bias photon-to-electron conversion efficiency (ABPE) calculations (Fig. 6d and Eq S10) reveal a maximum efficiency of approximately 0.04% at ~0.8 V vs RHE for BVO/rGO/FTO, indicating a slightly more favorable balance between bulk charge transport and surface reaction kinetics in this architecture. In contrast, rGO/BVO/FTO and pristine BVO/FTO reach their maximum ABPE at higher applied bias

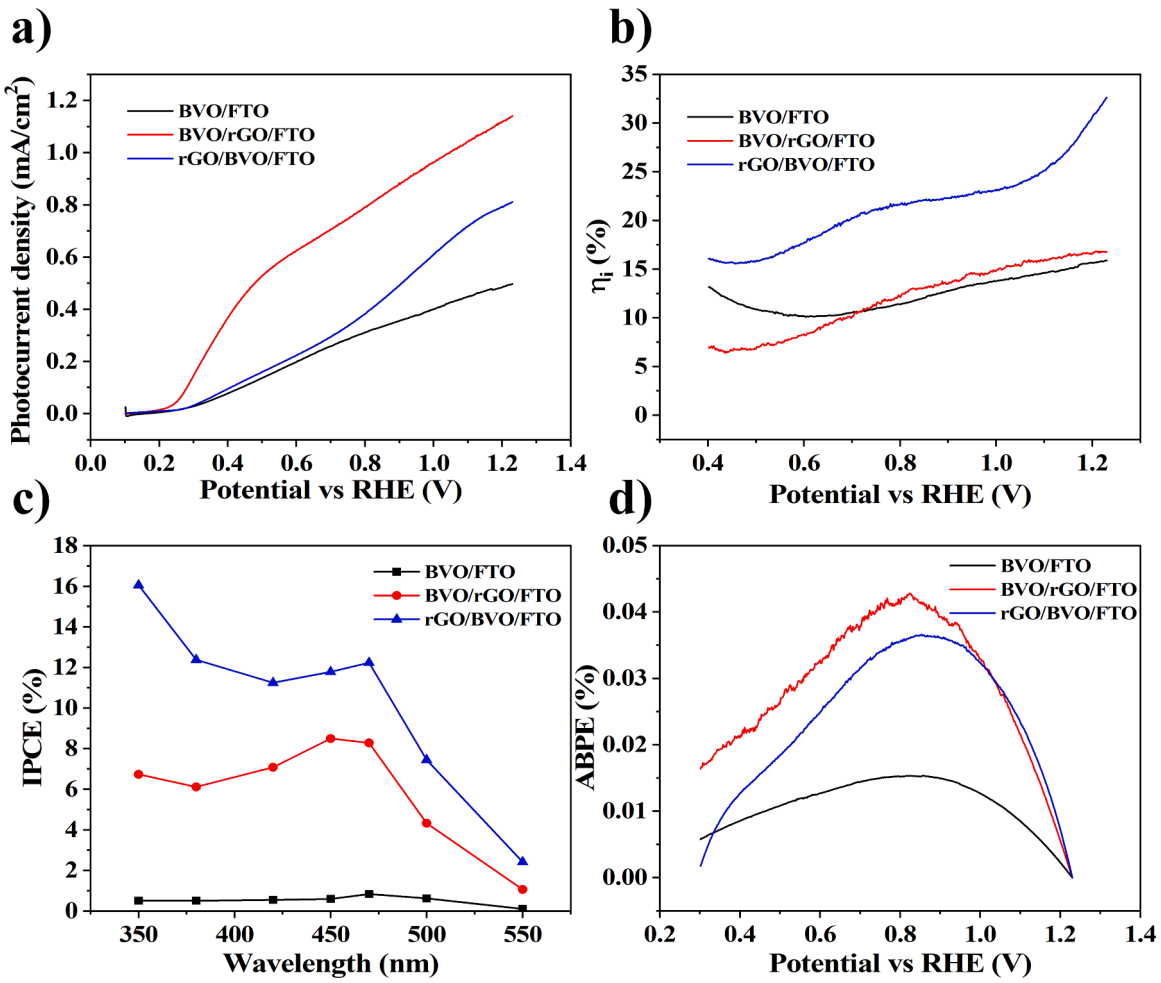

Fig. 6. a) LSV in 0.2 M sodium sulfite; b) charge transfer efficiency at the interface; c) IPCE and d) ABPE in the 0.1 M phosphate buffer of BVO/FTO, BVO/rGO/FTO, and rGO/BVO/FTO.

(~0.9 V vs RHE), with lower peak efficiencies of approximately 0.03% and 0.01%, respectively. Although the differences in ABPE between the rGO-modified photoanodes are modest, the shift of the efficiency maximum toward lower bias for BVO/rGO/FTO highlights the beneficial role of back-contact rGO in improving bulk charge separation and enabling more efficient utilization of absorbed photons under moderate applied bias. The obtained ABPE values remain lower than those reported for more extensively engineered BVO/rGO-based systems incorporating cocatalysts or highly optimized nanostructures, where ABPE values approaching or exceeding 1% have been achieved [17,58]. This difference likely originates from the absence of additional oxygen-evolution cocatalysts and the relatively compact morphology of the present hydrothermally synthesized films, which still limits overall charge-transport efficiency and interfacial water-oxidation kinetics.

Fig. 7 summarizes the optical transmission characteristics, light-harvesting efficiency, absorbed photon-to-current efficiency, and charge-transport behavior of pristine BVO and rGO-modified photoanodes. As shown in Fig. 7a, both rGO-containing electrodes exhibit a decrease in transmittance in the visible region compared to pristine BVO, indicating enhanced light attenuation upon rGO incorporation. Notably, the magnitude of the transmittance decrease is relatively small (on the order of a few percent), which is consistent with the presence of only a limited number of rGO layers. Considering that a single graphene-based layer typically induces an optical attenuation of ~2–3% in the visible region, the observed change suggests that the rGO coverage corresponds to only a few stacked layers, in agreement with the expected thin and partially discontinuous nature of the spin-coated rGO film [59]. Importantly, the position of the absorption edge remains essentially unchanged for all samples, suggesting that rGO does not significantly modify the intrinsic optical band structure of BVO. The reduced transmittance observed for rGO-modified electrodes is therefore attributed primarily to the optical absorption of rGO and additional light scattering at the rGO/BVO interfaces rather than to band gap narrowing.

To further assess whether rGO incorporation affects the electronic structure of BVO, optical band gaps were evaluated using Tauc analysis assuming both direct and indirect transitions (Figure S5), as there is not definitively established consensus regarding the optical transition character of BVO. Indirect band gap in the range of 2.26–2.32 eV and apparent direct band gap of 2.51–2.58 eV was obtained for all samples, in good agreement with literature values for monoclinic $BiVO_4$ [60–63]. No systematic shift in either the direct or indirect band gap is observed upon rGO incorporation within experimental uncertainty, confirming that rGO does not alter the bulk band structure of BVO.

The corresponding wavelength-dependent light-harvesting efficiency (LHE), derived from transmittance measurements (Eq. S7), is shown in Fig. 7b [64]. Compared to pristine BVO, both rGO-modified photoanodes exhibit moderately increased LHE below ~520 nm. Integration of the LHE over the absorption range yields maximum photocurrent densities (Eq. S8) (j_{abs}) of 5.6, 6.1, and 6.4 mA cm^{-2} for BVO/FTO, BVO/rGO/FTO, and rGO/BVO/FTO, respectively. The relatively small increase in j_{abs} (~10%) upon rGO incorporation, in this case, indicates that optical effects contribute only marginally to the overall photocurrent enhancement.

Despite these limited changes in light harvesting and band gap, a

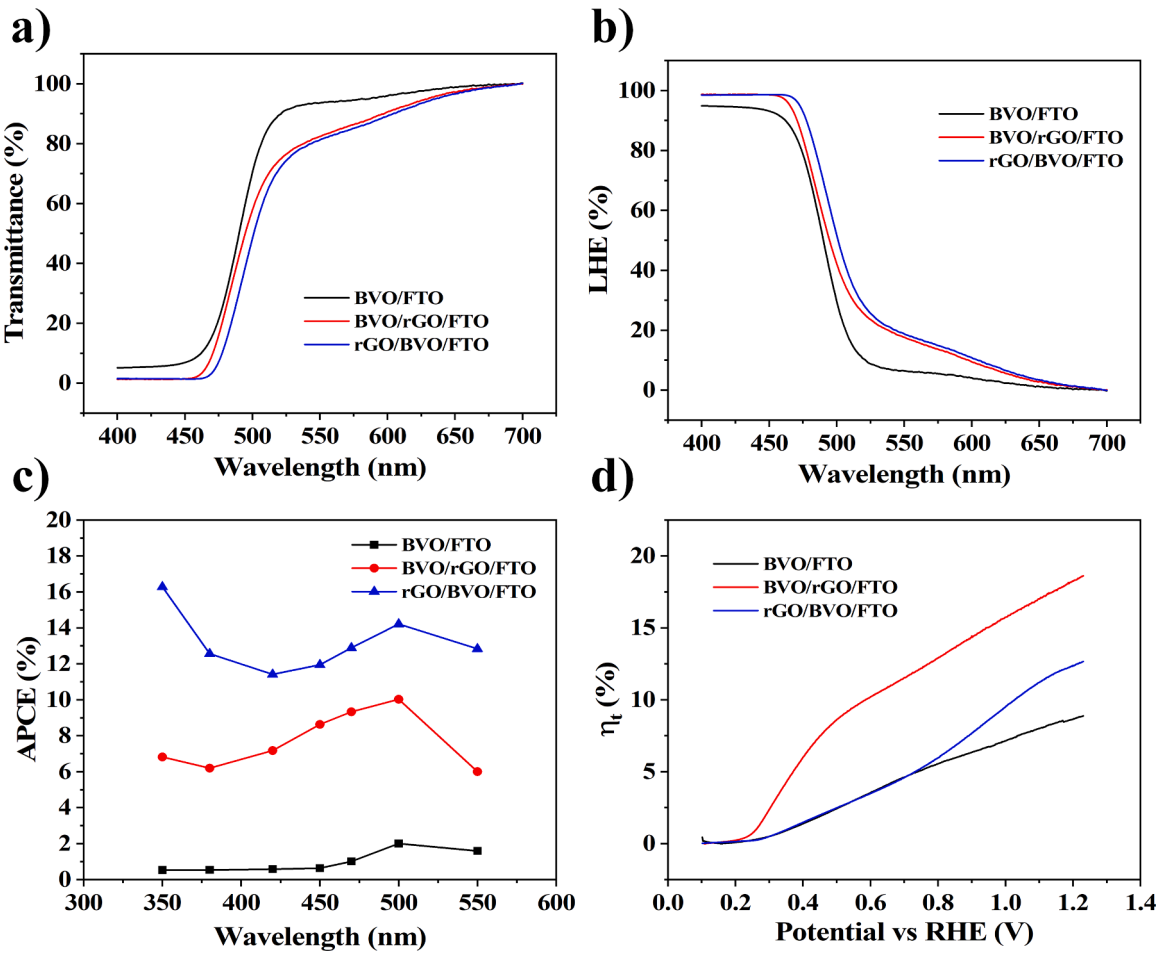

Fig. 7. a) Transmittance, b) Light harvesting efficiency, c) APCE and d) η_t of BVO/FTO, BVO/rGO/FTO and rGO/BVO/FTO.

pronounced enhancement in the absorbed photon-to-current efficiency (APCE) is observed upon rGO incorporation (Fig. 7c and Eq. S11). Pristine BVO/FTO exhibits very low APCE values (<2%) across the whole wavelength range, reflecting severe recombination losses. In contrast, both rGO-modified electrodes show substantially higher APCE values, with the rGO/BVO/FTO architecture exhibiting the highest APCE, reaching ~16% around 450–500 nm. The performance improvement in rGO-modified samples is believed to originate predominantly from improved charge separation and collection rather than from enhanced optical absorption or band-gap modification.

The potential-dependent charge-transport efficiency (η_t), shown in Fig. 7d, further supports this interpretation (Eq. S3-S6). Pristine BVO displays a gradual increase in η_t with applied potential, reaching only ~9% at 1.23 V vs RHE. In contrast, rGO-modified photoanodes exhibit significantly higher η_t, with BVO/rGO/FTO approaching ~19% at 1.23 V vs RHE. Importantly, normalization by j_{abs} confirms that this enhancement arises from reduced bulk recombination and more efficient electron extraction rather than increased photon absorption. The rGO/BVO/FTO architecture also improves η_t relative to pristine BVO, mostly in the potential region higher than 0.8 V vs RHE, consistent with its primary role in enhancing near-surface charge collection.

Additional insight into the enhanced charge-transport efficiency

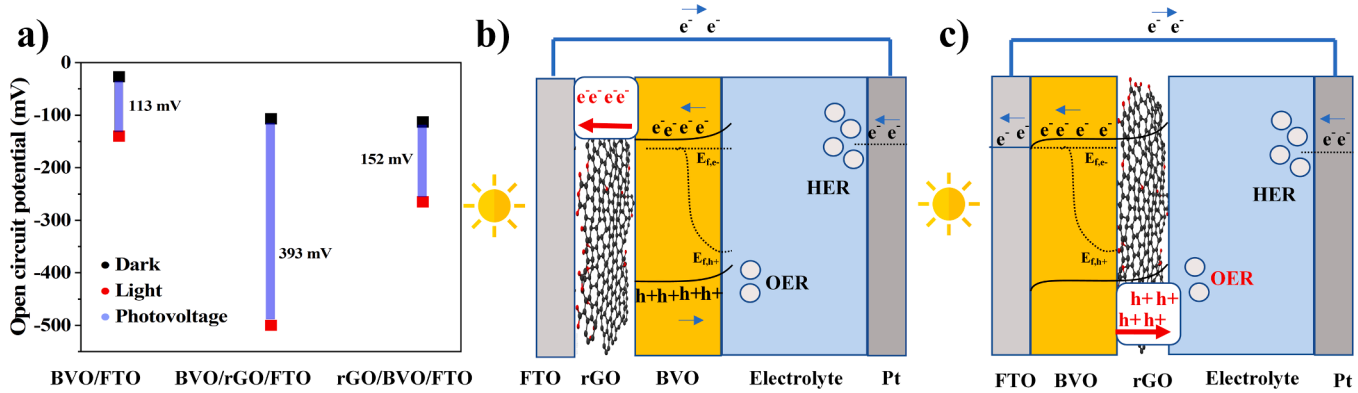

Fig. 8. a) Open circuit potential without (black rectangle) and with illumination (red rectangle) and photovoltage (purple) for BVO/FTO, BVO/rGO/FTO and rGO/BVO/FTO; Schematic representation of b) BVO/rGO/FTO and c) rGO/BVO/FTO where benefits of each heterostructure are emphasized by red color.

upon rGO incorporation is provided by open-circuit potential (OCP) measurements performed under dark and illuminated conditions (Fig. 8a). Pristine BVO exhibits a relatively small photovoltage (~110 mV), determined as the difference between OCP in dark and illuminated conditions, reflecting limited separation between electron and hole quasi-Fermi levels due to pronounced bulk recombination [65].

The significantly enhanced photovoltage (~400 mV) for BVO/rGO/FTO indicates more efficient accumulation of photogenerated electrons at the back contact and a higher degree of band bending within the $BiVO_4$ layer [37]. This behavior is consistent with the improved bulk charge transport and higher η_t values observed for BVO/rGO/FTO (Fig. 7d). The superior performance of this architecture can be attributed to favorable band alignment between rGO and $BiVO_4$. rGO possesses a work function typically in the range of ~4.4–4.8 eV, which closely matches the conduction band position of n-type $BiVO_4$, enabling efficient electron transfer from $BiVO_4$ into the rGO layer and subsequently to the FTO substrate [66–68]. This alignment reduces electron accumulation within the $BiVO_4$ bulk, suppresses recombination, and enhances the separation of quasi-Fermi levels under illumination. Also, as observed in Fig. 3b, reduced grain size can shorten carrier diffusion lengths and facilitate more efficient electron extraction toward the back contact [69].

In comparison, although the rGO/BVO/FTO architecture also exhibits an increased photovoltage relative to pristine BVO/FTO (~40 mV), the effect is less pronounced compared to the BVO/rGO/FTO. When rGO is deposited on the photoanode surface, its primary role is to modify surface of the BVO rather than to directly assist electron extraction to the back contact. Consequently, the improvement in photovoltage and transport efficiency is smaller, consistent with the reduced advantage of rGO/BVO/FTO under bulk-transport-limited conditions, such as in sodium sulfite electrolyte. Schematic representation of these phenomena is represented in Fig. 8b,c. Although the proposed charge-transfer mechanism is supported by photoelectrochemical, impedance, and surface characterization analyses together with literature comparison, future in-situ/operando spectroscopic investigations will be necessary to obtain a more comprehensive understanding of the interfacial charge-transfer and water oxidation processes in these systems.

4.4. Structural, morphological and surface analysis after PEC

After PEC operation, samples showed minimal changes in diffraction features (Figure S6), and morphology with maintained continuous coverage of the FTO substrate (Figure S7a, c, e). Nevertheless, high-magnification SEM images reveal the appearance of localized etched or roughened grains for all samples (Figure S7b, d, f). These features are attributed to localized photocorrosion and lattice destabilization associated with oxygen evolution under anodic bias in phosphate buffer.

Compared to the XPS spectra in Fig. 4, after PEC measurements, C 1 s spectrum of BVO/FTO exhibits an increase in the number and intensity of oxidized carbon components, with additional contributions appearing in the 286.5–288.9 eV range, indicating accumulation of surface hydroxylated and carbonate-like species during operation in aqueous electrolyte (Figure S8a). BVO/rGO/FTO shows a modest increase in oxidized carbon components, similar to pristine BVO/FTO (Figure S8b). Also, compared to the C 1 s spectrum of rGO/BVO/FTO in Fig. 4, after PEC, there is a further broadening and the appearance of new high-energy components (>292 eV), indicating chemical modification and partial oxidation of the surface-exposed rGO during photoelectrochemical operation (Figure S8c).

Similarly, analysis of O 1 s spectra of BVO/FTO and BVO/rGO/FTO, after PEC, show an increase in the relative intensity of hydroxylated and adsorbed oxygen components, reflecting changes at the surface including hydroxylation, and possible formation of oxygen-rich/deficient sites during water oxidation (Figure S8a, b) [70]. Similarly to the O 1 s spectra of rGO/BVO/FTO before PEC (Fig. 4c), Figure S8c shows a complex O 1 s spectrum, with multiple high-binding-energy components indicating increased surface oxidation and chemical instability of rGO under oxidative PEC conditions.

The Bi 4f and V 2p spectra show no significant shifts in binding energy or changes in spin–orbit splitting before and after PEC for any sample, confirming that bismuth and vanadium largely retain their Bi^{3+} and V^{5+} oxidation states.

Quantitative XPS analysis (Table S2) reveals pronounced surface non-stoichiometry for all photoanodes, with significant Bi enrichment relative to V compared to the ideal 1:1 $BiVO_4$ composition. Such Bi enrichment is commonly observed for hydrothermally grown $BiVO_4$ films and is typically attributed to preferential vanadium depletion or surface segregation of bismuth species during synthesis and thermal treatment [71,72]. Pristine BVO exhibits a Bi:V ratio of ~3.8 prior to PEC operation, which increases dramatically after PEC (Bi:V = 12) due to substantial vanadium depletion, indicating preferential V destabilization under anodic conditions in phosphate buffer. A similar Bi-rich surface is observed for BVO/rGO/FTO and rGO/BVO/FTO before PEC (Bi:V = 4.4 and 6.3, respectively), which becomes more Bi-dominated after PEC in the case of BVO/rGO/FTO (Bi:V = 8.3) while it decreases to 4.1 in the case of rGO/BVO/FTO probably as rGO acted as a protective layer, mitigating direct exposure of $BiVO_4$ to the electrolyte and suppressing vanadium loss. On the other hand, rGO/BVO/FTO shows high surface carbon content before PEC (≈70 at.%) due to rGO coverage, resulting in attenuated Bi and V signals. After PEC, the carbon content decreases (56 at.%) while oxygen increases markedly (to 40 at.%), consistent with partial oxidation of the surface rGO layer.

5. Conclusion

In summary, this study demonstrates that the photoelectrochemical performance of $BiVO_4$ photoanodes can be effectively tuned through the controlled integration of reduced graphene oxide in two distinct architectures, either beneath the $BiVO_4$ layer as a conductive back-contact interlayer or deposited on top of the semiconductor surface, highlighting electrode architecture as a key design parameter. Compared to pristine $BiVO_4$, both rGO-modified configurations exhibit significantly enhanced photocurrent densities and improved charge-transfer characteristics, with photocurrent densities increased by approximately 2.5 times under water oxidation conditions. Importantly, the two architectures provide distinct yet complementary advantages. Placement of rGO at the semiconductor–electrolyte interface (rGO/BVO/FTO) primarily enhances surface charge extraction leading to the highest photoelectrochemical activity at 1.23 V vs RHE in sodium phosphate buffer, with interfacial efficiencies exceeding 25–30% at anodic bias. However, although surface-exposed rGO significantly enhances the initial photoelectrochemical activity, it also compromises long-term operational stability, highlighting an inherent trade-off between performance enhancement and durability that must be carefully considered for practical applications. In contrast, incorporation of rGO at the back contact (BVO/rGO/FTO) predominantly improves bulk charge separation and electron extraction toward the FTO substrate, resulting in a nearly twofold increase in charge-transport efficiency, reaching values of approximately 19% at 1.23 V vs RHE under bulk-limited conditions. Spectroscopic and efficiency analyses further reveal that rGO integration enhances photon-to-current conversion across the visible spectrum, with absorbed photon-to-current efficiencies increasing from below 2% for pristine $BiVO_4$ to approximately 15–16% for rGO-modified photoanodes, while the optical band gap remains unchanged within experimental uncertainty. X-ray photoelectron spectroscopy suggests that the presence of rGO may influence the surface chemical environment and interfacial electronic interactions, which could contribute to the observed suppression of recombination and improved charge extraction.

Overall, these findings underscore the critical importance of spatially engineered rGO–oxide interfaces in governing charge separation, transport, and stability in ceramic photoelectrodes, which can be extended to other 2D materials as well. Rather than acting as a simple

additive, rGO fulfills architecture-dependent functional roles within the photoanode. The insights presented here provide a quantitative framework for the rational design of durable and efficient $BiVO_4$-based photoanodes and are readily extendable to other oxide semiconductors and 2D materials for solar-driven energy conversion.

CRediT authorship contribution statement

Marko Jelić: Writing – original draft, Methodology, Investigation, Formal analysis, Data curation, Conceptualization. **Zoran Jovanović:** Writing – review & editing, Validation, Methodology, Conceptualization. **Suraj Gupta:** Writing – review & editing, Formal analysis, Data curation. **Danica Bajuk-Bogdanović:** Writing – review & editing, Formal analysis, Data curation. **Srečo Škapin:** Writing – review & editing, Formal analysis, Data curation. **Zhao Liang:** Writing – review & editing. **Matjaž Spreitzer:** Writing – review & editing, Supervision. **Sonja Jovanović:** Writing – review & editing, Validation, Supervision, Methodology, Conceptualization.

Declaration of competing interest

The authors declare the following financial interests/personal relationships which may be considered as potential competing interests:

Marko Jelic reports financial support was provided by Journal of European Ceramic Society Trust. If there are other authors, they declare that they have no known competing financial interests or personal relationships that could have appeared to influence the work reported in this paper.

Acknowledgment

The research was financially supported by the Ministry of Science, Technological Development and Innovation (MoSTI) of the Republic of Serbia (Grants no. 451-03-33/2026-03/200017 and 451-03-33/2026-03/200146") and bilateral project of Serbia - Slovenia scientific collaboration (Grant no. 337-00-110/2023-05/28). This research was supported by the Science Fund of the Republic of Serbia, grant No. 6706, "Low-dimensional nanomaterials for energy storage and sensing applications: Innovation through synergy of action"- ASPIRE. The authors are grateful to the JECS Trust for funding the visit of Dr. Marko Jelić to the Advanced materials department at Jozef Stefan Institute as part of the JECS Trust mobility program (Contract No. 2025 488)." The authors would like to thank Damjan Vengust for conducting the SEM measurements, Dr. Željko Mravik for his assistance in the preparation of the schematics, and Dr. Jelena Maletaškić for her support related to the JECS grant. S. Gupta, S. Škapin, and M. Spreitzer acknowledge the Slovenian Research and Innovation Agency for financial support through research program P2-0091 and projects J7-50227, GC-0004, and HyBReED. S. Gupta also acknowledges the bilateral grant from IJS-CNR (2026–27).

Supplementary materials

Supplementary material associated with this article can be found, in the online version, at doi:10.1016/j.oceram.2026.101009.

References

[1] M. Walter, J. McKone, S. Boettcher, Q. Mi, E. Santori, N. Lewis, Solar Water Splitting Cells, Chem. Revews 110 (2010) 6446–6473.
[2] J.H. Kim, J.S. Lee, Elaborately modified BiVO4 photoanodes for solar water splitting, Adv Mater 31 (2019) e1806938, https://doi.org/10.1002/adma.201806938.
[3] Y. Park, K.J. Mc Donald, K.S. Choi, Progress in bismuth vanadate photoanodes for use in solar water oxidation, Chem. Soc. Rev. 42 (2013) 2321–2337, https://doi.org/10.1039/c2cs35260e.
[4] H.L. Tan, R. Amal, Y.H. Ng, Alternative strategies in improving the photocatalytic and photoelectrochemical activities of visible light-driven BiVO4: a review, J. Mater. Chem. A 5 (2017) 16498–16521, https://doi.org/10.1039/C7TA04441K.
[5] M. Jelić, E. Korneeva, D. Bajuk-Bogdanović, I. Pašti, J. Erčić, M. Stoiljković, Z. Jovanović, V. Skuratov, S. Jovanović, Correlation between phase composition and physicochemical properties in Cu-, Mo-, and W- doped bismuth vanadate, Ceram. Int. 50 (2024) 35583–35599, https://doi.org/10.1016/j.ceramint.2024.06.374.
[6] M. Jelić, Z. Jovanović, E. Korneeva, N. Daneu, S. Gupta, J. O'Connell, T. Vershinina, N. Kirilkin, O. Orelovich, I.S. Simatović, V. Skuratov, S. Jovanović, Defect engineering and opening of the ion tracks in the swift heavy ion irradiated thin films of bismuth vanadate: impact on the oxygen evolution reaction for solar water splitting, J. Mater. Chem. A 13 (2025) 17029–17041, https://doi.org/10.1039/D4TA09066G.
[7] S. Wang, D. Cui, W. Hao, Y. Du, Roles of cocatalysts on BiVO4 photoanodes for photoelectrochemical water oxidation: a minireview, Energy & Fuels 36 (2022) 11394–11403, https://doi.org/10.1021/acs.energyfuels.2c01391.
[8] A. Wang, S. Shen, Y. Zhao, W. Wu, Preparation and characterizations of BiVO4/reduced graphene oxide nanocomposites with higher visible light reduction activities, J. Colloid Interface Sci. 445 (2015) 330–336, https://doi.org/10.1016/j.jcis.2015.01.017.
[9] T. Soltani, A. Tayyebi, B.-K. Lee, Efficient promotion of charge separation with reduced graphene oxide (rGO) in BiVO4/rGO photoanode for greatly enhanced photoelectrochemical water splitting, Sol. Energy Mater. Sol. Cells 185 (2018) 325–332, https://doi.org/10.1016/j.solmat.2018.05.050.
[10] R. Tarcan, O. Todor-Boer, I. Petrovai, C. Leordean, S. Astilean, I. Botiz, Reduced graphene oxide today, J. Mater. Chem. C 8 (2020) 1198–1224, https://doi.org/10.1039/C9TC04916A.
[11] N. Zhang, Y. Zhang, Y.-J. Xu, Recent progress on graphene-based photocatalysts: current status and future perspectives, Nanoscale 4 (2012) 5792, https://doi.org/10.1039/C2NR31480K.
[12] A. Mondal, A. Prabhakaran, S. Gupta, V.R. Subramanian, Boosting photocatalytic activity using reduced graphene oxide (RGO)/semiconductor nanocomposites: issues and future scope, ACS Omega 6 (2021) 8734–8743, https://doi.org/10.1021/acsomega.0c06045.
[13] M.A. Ahmed, A.A. Mohamed, Recent progress in semiconductor/graphene photocatalysts: synthesis, photocatalytic applications, and challenges, RSC Adv. 13 (2023) 421–439, https://doi.org/10.1039/D2RA07225D.
[14] D. Petković, H.-C. Ho, L. Bučar, J. Kovač, D. Vengust, S. Jovanović, M. Spreitzer, Z. Jovanović, Engineering charge transfer in PLD-grown STO thin films on Si(001) by an rGO interlayer for photoelectrochemical hydrogen evolution, ACS Appl. Energy Mater. 8 (2025) 18234–18245, https://doi.org/10.1021/acsaem.5c03161.
[15] Y.H. Ng, A. Iwase, A. Kudo, R. Amal, Reducing graphene oxide on a visible-light BiVO4 photocatalyst for an enhanced photoelectrochemical water splitting, J. Phys. Chem. Lett. 1 (2010) 2607–2612, https://doi.org/10.1021/jz100978u.
[16] T. Soltani, A. Tayyebi, B.-K. Lee, Photolysis and photocatalysis of tetracycline by sonochemically heterojunctioned BiVO4/reduced graphene oxide under visible-light irradiation, J. Environ. Manage. 232 (2019) 713–721, https://doi.org/10.1016/j.jenvman.2018.11.133.
[17] H. Chen, S. Wang, J. Wu, X. Zhang, J. Zhang, M. Lyu, B. Luo, G. Qian, L. Wang, Identifying dual functions of rGO in a BiVO4/rGO/NiFe-layered double hydroxide photoanode for efficient photoelectrochemical water splitting, J. Mater. Chem. A 8 (2020) 13231–13240, https://doi.org/10.1039/D0TA04572A.
[18] T.-M. Cheng, Y.-R. Wang, Y.-H. Chiu, R.-J. Chung, C. Kongvarhodom, M. Saukani, S. Yougbaré, H.-M. Chen, L.-Y. Lin, Alkaline modified bismuth vanadate coupled with reduced graphene oxide as efficient photoelectrochemical catalysts for water oxidation, Int. J. Hydrogen Energy 98 (2025) 1226–1234, https://doi.org/10.1016/j.ijhydene.2024.12.139.
[19] Y. Wang, W. Wang, H. Mao, Y. Lu, J. Lu, J. Huang, Z. Ye, B. Lu, Electrostatic self-assembly of BiVO4–Reduced graphene oxide nanocomposites for highly efficient visible light photocatalytic activities, ACS Appl. Mater. Interfaces 6 (2014) 12698–12706, https://doi.org/10.1021/am502700p.
[20] T. Wang, C. Li, J. Ji, Y. Wei, P. Zhang, S. Wang, X. Fan, J. Gong, Reduced graphene oxide (rGO)/BiVO4 composites with maximized interfacial coupling for visible lght photocatalysis, ACS Sustain. Chem. Eng. 2 (2014) 2253–2258, https://doi.org/10.1021/sc5004665.
[21] H.L. Tan, H.A. Tahini, X. Wen, R.J. Wong, X. Tan, A. Iwase, A. Kudo, R. Amal, S. C. Smith, Y.H. Ng, Interfacing BiVO4 with reduced graphene oxide for enhanced photoactivity: a tale of facet dependence of electron shuttling, Small 12 (2016) 5295–5302, https://doi.org/10.1002/smll.201601536.
[22] M. Shao, S. Hou, X. Fu, X. Li, Y. Chen, P.-Y. Su, Y. Huang, Analytical investigation of charge carrier separation in photoelectrochemical water splitting: multi-Scale methods and emerging trends, TrAC Trends Anal. Chem. 196 (2026) 118672, https://doi.org/10.1016/j.trac.2026.118672.
[23] M. Shao, S. Hou, X. Li, H. Yang, Y. Huang, Z.-Q. Liu, Dual-channel charge manipulation for enhancing charge separation and transfer kinetics in BiVO4 photoanodes, ACS Catal 16 (2026) 4017–4027, https://doi.org/10.1021/acscatal.5c09177.
[24] Y. Chen, J. Huang, J. Zhou, X. Li, H. Yang, Y. Huang, Combinational effect of NiFeOx/Tb(OH)x as hole extractor for enhanced charges separation and stability of BiVO4 photoanode for solar water splitting, Mater. Today Adv. 25 (2025) 100554, https://doi.org/10.1016/j.mtadv.2024.100554.
[25] Z.-Y. You, H. Cheshideh, A.A. Jagtap, H.-C. Chen, R.-J. Chung, L.-Y. Lin, Orbital engineering of phosphidized CoFe oxide/BiVO4 heterojunctions for scavenger-free PEC water splitting revealed by DFT and multimodal spectroscopy, ACS Catal. 16 (2026) 5856–5873, https://doi.org/10.1021/acscatal.5c09268.

[26] P. Lv, Z. Xie, G. Yi, Y. Zhao, M. Shang, X. Yang, S. Wen, Z. Jing, Q. Wang, D. Song, P. Tang, Enhanced photoelectrochemical water splitting of BiVO4 photoanode via synergistic effects of polycarbazole hole transport layer and NiFeOOH cocatalyst, ACS Catal 16 (2026) 6649–6662, https://doi.org/10.1021/acscatal.5c09061.
[27] Z. Jovanovic, D. Bajuk-Bogdanović, S. Jovanović, Ž. Mravik, J. Kovač, I. Holclajtner-Antunović, M. Vujković, The role of surface chemistry in the charge storage properties of graphene oxide, Electrochim. Acta 258 (2017) 1228–1243, https://doi.org/10.1016/j.electacta.2017.11.178.
[28] M.D. Archer, Genesis of the Nernst equation. Electrochem. Past Present, American Chemical Society, 1989, pp. 115–126, https://doi.org/10.1021/bk-1989-0390.ch008. SE–8.
[29] R H.D. Frost, M. Weier, W. Martens, Raman spectroscopy of three polymorphs of BiVO4: clinobisvanite, dreyerite and pucherite, with comparisons to (VO4)3-bearing minerals: namibite, pottsite and schumacherite, J. Raman Spectrosc. 37 (2006) 722–732, https://doi.org/10.1002/jrs.1499.
[30] F.D. Hardcastle, I.E. Wachs, H. Eckert, D.A. Jefferson, Vanadium(V) environments in bismuth vanadates: a structural investigation using Raman spectroscopy and solid state 51V NMR, J. Solid State Chem. 90 (1991) 194–210, https://doi.org/10.1016/0022-4596(91)90135-5.
[31] N.M.S. Hidayah, W.-W. Liu, C.-W. Lai, N.Z. Noriman, C.-S. Khe, U. Hashim, H. C. Lee, Comparison on graphite, graphene oxide and reduced graphene oxide: synthesis and characterization, AIP Conf. Proc. 1892 (2017) 150002, https://doi.org/10.1063/1.5005764.
[32] A.C. Ferrari, J. Robertson, Interpretation of Raman spectra of disordered and amorphous carbon, Phys. Rev. B 61 (2000) 14095–14107, https://doi.org/10.1103/PhysRevB.61.14095.
[33] C.-Y. Kim, D.-H. Riu, Raman scattering, electrical and optical properties of fluorine-doped tin oxide thin films with (200) and (301) preferred orientation, Mater. Chem. Phys. 148 (2014) 810–817, https://doi.org/10.1016/j.matchemphys.2014.08.055.
[34] S. Tokunaga, H. Kato, A. Kudo, Selective preparation of monoclinic and tetragonal BiVO4 with scheelite structure and their photocatalytic properties, Chem. Mater. 13 (2001) 4624–4628, https://doi.org/10.1021/cm0103390.
[35] B.-C. Xiao, L.-Y. Lin, J.-Y. Hong, H.-S. Lin, Y.-T. Song, Synthesis of a monoclinic BiVO4 nanorod array as the photocatalyst for efficient photoelectrochemical water oxidation, RSC Adv. 7 (2017) 7547–7554, https://doi.org/10.1039/C6RA28262H.
[36] S. Wang, P. Chen, J.H. Yun, Y. Hu, L. Wang, An electrochemically treated BiVO4 photoanode for efficient photoelectrochemical water splitting, Angew. Chem. Int. Ed. Engl. 56 (2017) 8500–8504, https://doi.org/10.1002/anie.201703491.
[37] D. Li, Y. Liu, W. Shi, C. Shao, S. Wang, C. Ding, T. Liu, F. Fan, J. Shi, C. Li, Crystallographic-orientation-dependent charge separation of BiVO4 for solar water oxidation, ACS Energy Lett. 4 (2019) 825–831, https://doi.org/10.1021/acsenergylett.9b00153.
[38] M. Li, G. Xu, Z. Guan, Y. Wang, H. Yu, Y. Yu, Synthesis of Ag/BiVO4/rGO composite with enhanced photocatalytic degradation of triclosan, Sci. Total Environ. 664 (2019) 230–239, https://doi.org/10.1016/j.scitotenv.2019.02.027.
[39] Y. Zhang, Y. Guo, Q. Du, H. Duan, Y. Chen, H. Li, H. Liu, Oxygen vacancies induced self-assembling synthesis of V4+-BiVO4/rGO core-shell nanorods with enhanced water splitting efficiency and superior sewage purification capability, Appl. Catal. A Gen. 526 (2016) 105–112, https://doi.org/10.1016/j.apcata.2016.08.012.
[40] S.-H. Yoon, D.-W. Park, K.-S. Kim, Preparation of WO3, BiVO4 and reduced graphene oxide composite thin films and their photoelectrochemical performance, Korean J. Chem. Eng. 34 (2017) 3220–3225, https://doi.org/10.1007/s11814-017-0237-4.
[41] L.G. Guex, B. Sacchi, K.F. Peuvot, R.L. Andersson, A.M. Pourrahimi, V. Ström, S. Farris, R.T. Olsson, Experimental review: chemical reduction of graphene oxide (GO) to reduced graphene oxide (rGO) by aqueous chemistry, Nanoscale 9 (2017) 9562–9571, https://doi.org/10.1039/C7NR02943H.
[42] J.A. Quezada Renteria, C. Ruiz-Garcia, T. Sauvage, L.F. Chazaro-Ruiz, J.R. Rangel-Mendez, C.O. Ania, Photochemical and electrochemical reduction of graphene oxide thin films: tuning the nature of surface defects, Phys. Chem. Chem. Phys. 22 (2020) 20732–20743, https://doi.org/10.1039/D0CP02053B.
[43] S. Wang, T. He, P. Chen, A. Du, K.K. Ostrikov, W. Huang, L. Wang, Situ formation of oxygen vacancies achieving near-complete charge separation in planar BiVO(4) photoanodes, Adv. Mater. 32 (2020) e2001385, https://doi.org/10.1002/adma.202001385.
[44] Y. Hermans, C. Olivier, H. Junge, A. Klein, W. Jaegermann, T. Toupance, Sunlight selective photodeposition of CoOx(OH)y and NiOx(OH)y on truncated bipyramidal BiVO4 for highly efficient photocatalysis, ACS Appl. Mater. Interfaces 12 (2020) 53910–53920, https://doi.org/10.1021/acsami.0c14624.
[45] A. Roy, P. Majumdar, P. Sengupta, S. Kundu, S. Shinde, A. Jha, K. Pramanik, H. Saha, A photoelectrochemical supercapacitor based on a single BiVO4-RGO bilayer photocapacitive electrode, Electrochim. Acta 329 (2020) 135170, https://doi.org/10.1016/j.electacta.2019.135170.
[46] C.S. Yaw, W.C. Ng, Q. Ruan, J. Tang, A.K. Soh, M.N. Chong, Tuning of reduced graphene oxide thin film as an efficient electron conductive interlayer in a proven heterojunction photoanode for solar-driven photoelectrochemical water splitting, J. Alloys Compd. 817 (2020) 152721, https://doi.org/10.1016/j.jallcom.2019.152721.
[47] M.C. Cotto, J. Ducongé, F. Díaz, I. García, C. Neira, C. Morant, F. Márquez, Photoresponsive TiO2/graphene hybrid electrodes for dual-function supercapacitors with integrated environmental sensing capabilities, Batteries 11 (2025) 460, https://doi.org/10.3390/batteries11120460.
[48] B.D. Nguyen, I.-H. Choi, J.-Y. Kim, Strategies for enhancing BiVO4 photoanodes for PEC water splitting: a State-of-the-art review, Nanomaterials 15 (2025) 1494, https://doi.org/10.3390/nano15191494.
[49] Q. Shi, X. Song, H. Wang, Z. Bian, Enriched photoelectrochemical performance of phosphate doped BiVO4 photoelectrode by coupling FeOOH and rGO, J. Electrochem. Soc. 165 (2018) H3018–H3027, https://doi.org/10.1149/2.0021804jes. H3018.
[50] S. Zhang, T. Duan, D. Yan, H. Yang, L. Cheng, Y. Pei, K. You, H. Luo, Hole transfer layer of glucose-derived carbon enabled rapid charge transfer and hole storage for efficient water splitting, Chem. Eng. J. 486 (2024) 150176, https://doi.org/10.1016/j.cej.2024.150176.
[51] Y. Ma, S.R. Pendlebury, A. Reynal, F. Le Formal, J.R. Durrant, Dynamics of photogenerated holes in undoped BiVO4 photoanodes for solar water oxidation, Chem. Sci. 5 (2014) 2964–2973, https://doi.org/10.1039/c4sc00469h.
[52] B. Klahr, S. Gimenez, F. Fabregat-Santiago, T. Hamann, J. Bisquert, Water oxidation at hematite photoelectrodes: the role of surface states, J. Am. Chem. Soc. 134 (2012) 4294–4302, https://doi.org/10.1021/ja210755h.
[53] A. Hankin, F.E. Bedoya-Lora, J.C. Alexander, A. Regoutz, G.H. Kelsall, Flat band potential determination: avoiding the pitfalls, J. Mater. Chem. A 7 (2019) 26162–26176, https://doi.org/10.1039/c9ta09569a.
[54] S.S. Patil, M.G. Mali, M.A. Hassan, D.R. Patil, S.S. Kolekar, S.-W. Ryu, One-pot in situ hydrothermal growth of BiVO4/Ag/rGO hybrid architectures for solar water splitting and environmental remediation, Sci. Rep. 7 (2017) 8404, https://doi.org/10.1038/s41598-017-08912-z.
[55] Y. Zhang, L. Xu, B. Liu, X. Wang, T. Wang, X. Xiao, S. Wang, W. Huang, Engineering BiVO4 and oxygen evolution cocatalyst interfaces with rapid hole extraction for photoelectrochemical water splitting, ACS Catal. 13 (2023) 5938–5948, https://doi.org/10.1021/acscatal.3c00444.
[56] M. Abdollahi, Z. Sadeghian, E. Akbarinezhad, K. Sadeghian, A. Rahimi, Boosted visible light photoelectrochemical water splitting performance by tailoring a nanostructure of BiVO4/rGO and BiVO4/g-C3N4 composites, Chem. Inorg. Mater. 6 (2025) 100103, https://doi.org/10.1016/j.cinorg.2025.100103.
[57] S. Jia, L. Zha, X. Zhao, S. Bai, K. Tian, Y. Feng, rGO modified in situ transformed Bi2S3/BiVO4 heterostructure for photoelectrochemical water oxidation, Electrochim. Acta 543 (2025) 147648, https://doi.org/10.1016/j.electacta.2025.147648.
[58] X. Li, S. Hou, X. Xie, H. Yang, Y. Huang, Lattice strain engineering via electrochemical treatment boosts solar water oxidation of BiVO4 through accelerated intermediate conversion, J. Catal. 453 (2026) 116540, https://doi.org/10.1016/j.jcat.2025.116540.
[59] R.R. Nair, P. Blake, A.N. Grigorenko, K.S. Novoselov, T.J. Booth, T. Stauber, N.M. R. Peres, A.K. Geim, Fine structure constant defines visual transparency of graphene, Science 320 (80–) (2008) 1308, https://doi.org/10.1126/science.1156965.
[60] A. Walsh, Y. Yan, M.N. Huda, M.M. Al-Jassim, S.-H. Wei, Band edge electronic structure of BiVO4: elucidating the role of the Bi s and V d orbitals, Chem. Mater. 21 (2009) 547–551, https://doi.org/10.1021/cm802894z.
[61] X. Wu, J. Zhao, L. Wang, M. Han, M. Zhang, H. Wang, H. Huang, Y. Liu, Z. Kang, Carbon dots as solid-state electron mediator for BiVO4/CDs/CdS Z-scheme photocatalyst working under visible light, Appl. Catal. B Environ. 206 (2017) 501–509, https://doi.org/10.1016/j.apcatb.2017.01.049.
[62] J.K. Cooper, S. Gul, F.M. Toma, L. Chen, Y.-S. Liu, J. Guo, J.W. Ager, J. Yano, I. D. Sharp, Indirect bandgap and optical properties of monoclinic bismuth vanadate, J. Phys. Chem. C 119 (2015) 2969–2974, https://doi.org/10.1021/jp512169w.
[63] Z. Zhao, W. Luo, Z. Li, Z. Zou, Density functional theory study of doping effects in monoclinic clinobisvanite BiVO4, Phys. Lett. A 374 (2010) 4919–4927, https://doi.org/10.1016/j.physleta.2010.10.014.
[64] Zhebo Chen, Huyen N. Dinh, Eric Miller, Photoelectrochemical Water Splitting Standards, Experimental methods and Protocols, Springer, New York, NY, 2013, https://doi.org/10.1007/978-1-4614-8298-7.
[65] C. Du, X. Yang, M.T. Mayer, H. Hoyt, J. Xie, G. McMahon, G. Bischoping, D. Wang, Hematite-based water splitting with low turn-on voltages, Angew. Chem. Int. Ed. Engl. 52 (2013) 12692–12695, https://doi.org/10.1002/anie.201306263.
[66] M. Kumar, M.N.M. Ansari, I. Boukhris, M.S. Al-Buriahi, Z.A. Alrowaili, N. Alfryyan, P. Thomas, R. Vaish, Sonophotocatalytic dye degradation using rGO-BiVO4 composites, Glob. Challenges 6 (2022) 2100132, https://doi.org/10.1002/gch2.202100132.
[67] S. Naghdi, H.Y. Song, A. Várez, K.Y. Rhee, S.W. Kim, Engineering the electrical and optical properties of graphene oxide via simultaneous alkali metal doping and thermal annealing, J. Mater. Res. Technol. 9 (2020) 15824–15837, https://doi.org/10.1016/j.jmrt.2020.10.016.
[68] Y. Hermans, A. Klein, K. Ellmer, R. van de Krol, T. Toupance, W. Jaegermann, Energy-band alignment of BiVO4 from photoelectron spectroscopy of solid-State interfaces, J. Phys. Chem. C 122 (2018) 20861–20870, https://doi.org/10.1021/acs.jpcc.8b06241.
[69] M. Kölbach, H. Hempel, K. Harbauer, M. Schleuning, A. Petsiuk, K. Höflich, V. Deinhart, D. Friedrich, R. Eichberger, F.F. Abdi, R. van de Krol, Grain boundaries limit the charge carrier transport in pulsed laser deposited α-SnWO4 thin film photoabsorbers, ACS Appl. Energy Mater. 3 (2020) 4320–4330, https://doi.org/10.1021/acsaem.0c00028.
[70] F.M. Toma, J.K. Cooper, V. Kunzelmann, M.T. McDowell, J. Yu, D.M. Larson, N. J. Borys, C. Abelyan, J.W. Beeman, K.M. Yu, J. Yang, L. Chen, M.R. Shaner, J. Spurgeon, F.A. Houle, K.A. Persson, I.D. Sharp, Mechanistic insights into

chemical and photochemical transformations of bismuth vanadate photoanodes, Nat. Commun. 7 (2016) 12012, https://doi.org/10.1038/ncomms12012.
[71] M. Lamers, S. Fiechter, D. Friedrich, F.F. Abdi, R. van de Krol, Formation and suppression of defects during heat treatment of BiVO4 photoanodes for solar water splitting, J. Mater. Chem. A 6 (2018) 18694–18700, https://doi.org/10.1039/C8TA06269B.
[72] L. Chen, E. Alarcón-Lladó, M. Hettick, I.D. Sharp, Y. Lin, A. Javey, J.W. Ager, Reactive sputtering of bismuth vanadate photoanodes for solar water splitting, J. Phys. Chem. C 117 (2013) 21635–21642, https://doi.org/10.1021/jp406019r.